VILNIUS UNIVERSITY
FACULTY OF PHYSICS
LASER RESEARCH CENTER

Aleksandras Kondratas

DEBRIS REMOVAL TECHNIQUES FOR PICOSECOND LASER BOTTOM-UP MILLING OF FUSED SILICA

Bachelor's thesis

Study program – light engineering

Student	Aleksandras Kondratas
Work supervisor	dokt. Miglė Mackevičiūtė
Reviewer	Evaldas Kažukauskas
Center director	Dr. Dalia Kaškelytė

Vilnius 2024

Contents

Introduction:

Micromachining is invaluable for state-of-the-art manufacturing technologies. To realize microstructure feature sizes in the range of sub-micron to tens of microns and aspect ratios of 0.1 up to more than 10 [1], [2] novel machining techniques are needed. High aspect ratios in channels serve to connect micro-components within microfluidic devices, supporting the necessity for the formation of channels from materials possessing excellent optical, isolation, and thermal properties [1]. Materials like silicon and glass are therefore used, due to the mentioned properties and flexibility via different types of glass available. Produced channels and other parts have a wide range of applications [1], such as optical storage devices, micro-electro-mechanical-systems MEMS devices like piezoresistive pressure sensors, capillary nozzles [3], and others.

Laser milling is preferred over other milling techniques because it allows the formation of high aspect ratio channels with high throughput [1], [2]. The laser beam can be focused into a spot smaller than any mechanical tool, and since lasers have no physical contact with the workpiece, they don't wear out. With the addition of nonlinear phenomena, the drawbacks of typical thermal processes, such as heat-affected zones and cracking can be mitigated [2]. Longer laser wavelengths than UV, which is needed for direct ablation of fused silica, can be utilized to mill transparent media due to nonlinear phenomena [4]. A large market provides lasers with around 1 μm wavelength and pulse duration from nanoseconds to femtoseconds [5]. Wavelengths in the visible spectrum could be used via second or higher-order harmonic generation but at a loss to the power due to imperfect conversion of the crystals. The longer (ns) pulses typically provide higher throughput but at an increased heat-affected zone (HAZ) and rougher surface finish (Ra ~3 μm) [6]. Shorter picosecond pulses can enhance quality (Ra ~1 μm) [6], [7].

Milling with a top-down technique produces walls with an angle and milling efficiency suffers due to plasma shielding [8]. These effects can be mitigated using the bottom-up technique that allows for milled channels to have parallel walls and reduced plasma shielding since the debris does not go in the laser beam path [6], [8]. Consequently, higher aspect ratio channels can be formed using bottom-up machining [8]. To form deeper channels debris has to be removed from the milling area. Therefore, additional debris removal methods, such as airflow or water, are employed which can also increase the milled depth [6], [9].

This work aimed to investigate channel milling using 1064 nm wavelength picosecond pulses focused on the rear side of the fused silica with additional debris removal methods.

Theory part:

Linear absorption:

Photons can be absorbed in various media, thus resulting in energy transfer [10]. Absorption in media can arise from impurities and defects called extrinsic absorption or from the properties of pure material – intrinsic absorption. Semiconductors and dielectrics have empty states between the conduction and valance band and its magnitude is called bandgap, typically expressed in electron volts eV. For such materials, absorption only occurs when photon energy exceeds the bandgap. For example, fused silica (FS) has a relatively big bandgap of 9 eV [11], which equates to about 137 nm, requiring lasers in the far UV range. As an alternative, lasers with wavelengths above 4 μm could be used for FS as the transmission approaches 0% [12] due to the absorption of –OH vibrations [13]. Absorption causes electrons to be promoted from valance to the conduction band. Linear absorption can be described by formula (1), here *I(z)* is the light intensity after passing a material of thickness *z*, *R* is the surface reflection coefficient, and α is the absorption coefficient. The linear absorption coefficient is independent of optical intensity as opposed to nonlinear which is dependent on higher orders of intensity [10].

$$I(z) = I(1-R)e^{-\alpha z} = I_0 e^{-\alpha z} \tag{1}$$

Nonlinear absorption:

To achieve absorption in transparent materials at photon energies lower than UV, it is necessary to achieve nonlinear absorption, which happens at higher intensities and can manifest as different phenomena.

Materials have dielectric polarizability which can be expanded through the electric field power series formula (2). This represents the electric field's magnitude required to induce orders of nonlinear processes [14].

$$P(t) = \varepsilon_0 \chi^{(1)} E(t) + \varepsilon_0 \chi^{(2)} E^2(t) + \varepsilon_0 \chi^{(3)} E^3(t) + \dots \tag{2}$$

Here $\chi^{(2)}$ and $\chi^{(3)}$ are second and third-order coefficients of nonlinear influence, ε_0 is vacuum permittivity, and *E* is the electric field. The magnitude of the coefficients varies significantly [14].

$$\chi^{(1)} \approx \frac{\pi}{2},$$
$$\chi^{(2)} \approx 2\times10^{-12}\ \mathrm{m/V},$$
$$\chi^{(3)} \approx 4\times10^{-24}\ \mathrm{m^2/V^2}. \tag{3}$$

Higher orders follow the same dependence and therefore have an even smaller influence, requiring much higher intensities. Second-order nonlinear phenomena can only occur in dielectric crystals with non-centrosymmetric properties, while third-order nonlinear phenomena can occur in any media [14]. From formulas (2) and (3) it follows that to have nonlinear polarizability sufficiently large radiation intensity is required [14].

Large radiation intensity can result in the simultaneous absorption of two or multiple photons of lower energy than the bandgap. Simultaneous absorption can occur in a few configurations. Single beam, where photons of frequency ω excite an electron to a virtual level, for example, 2 photons to $2\hbar\omega$ excited state. Multiple beams, where some or all photons are of different energy, the resulting sum is equivalent to the excited state energy [4]. The intensity needed for

multiphoton absorption to occur is explained by formula (4). Here $\beta^{(K)}$ is the K-th order nonlinear absorption coefficient (K = $E_g/\hbar\omega$) [14].

$$\frac{dI}{dz} = -(\alpha + \beta^{(K)} I^{K-1})I. \quad (4)$$

Another way to look at nonlinear absorption is through the Keldysh model [15], [16]. Adiabaticity γ is the most important parameter in the Keldysh model and it is described by formula (5). Here ε and ω are the strength and the frequency of the electric field, t is the time of electron escape by tunneling ($\omega_t = \frac{1}{t}$), m is the reduced mass, and e is the electron charge.

$$\gamma = \frac{\omega\sqrt{2mE_g}}{e\varepsilon}. \quad (5)$$

$$\omega_t = \frac{e\varepsilon}{\sqrt{2mE_g}}. \quad (6)$$

$$\gamma = \omega t. \quad (7)$$

When γ » 1 multiphoton absorption is prevalent and the electric field increases, when γ « 1 it turns to tunneling. Tunnelling describes electrons going through a potential barrier in an external field which typically prevents movement. An important feature of tunneling is that it can be considered free of inertia; therefore, maintaining a high probability of tunneling up to very high frequencies [15]. This is because tunneling time is determined by electron free flight time across the barrier. Therefore, the tunneling effect is defined by electron velocity, formula (6). In conclusion, adiabaticity can be acquired as a product of field frequency and the time it takes for an electron to escape the atom by tunneling, formula (7) [15].

For avalanche ionization to occur photo-initiation is needed. Free carriers are generated whose energy can increase through inverse Bremsstrahlung absorption, and photon absorption through collision by free carriers [17]. They can then collide with other electrons liberating them and feeding the process. When this process is dominant free carriers are generated exponentially with time. However, for the process to begin a population of free carriers is required. Avalanche ionization is dominant for 1 ps or longer laser pulse durations [17]. Making it the primary absorption mechanism in this work.

Optical damage and laser milling:

Absorbed photons transfer energy to the material, resulting in the introduction of either mechanical stress, which can lead to microcracks, or melting [1]. However, it is not trivial to achieve milling for glass due to it being transparent for a wide range of wavelengths. Laser with wavelength in extreme UV or far IR could be used for direct laser ablation, of which CO_2 laser, commonly emitting at 10.6 μm wavelength, is widely used for industrial applications [1]. Alternatively, a laser with high peak intensities could be used to achieve nonlinear phenomena. Through which absorption and ultimately ablation occurs due to the build-up of free electrons [18]. At critical free-electron density dielectrics break down and the plasma becomes reflective and absorbent after it is exceeded [18]. After less than 10 ps after the pulse, the electron energy starts to relax which is the cause of damage and melting [18], [19]. Electron relaxation and ultimately temperature relaxation happen due to electron-phonon collisions in the range of picoseconds [19]. The molten material expands which results in material removal from the irradiation site, this can last up to a nanosecond scale [19]. The size of the milled area or damage depends on the amount of energy absorbed [19].

Optical damage could be caused to the surface near the machined area due to laser beam transmission and propagation through the tapered sidewalls, when the top-down technique is used, causing intra-volume or speckle modifications [6]. At the same time, the sides of the Gaussian beam constantly add energy that is insufficient for ablation contributing to the HAZ [20]. The aforementioned damage was the result of electronic damage, where atomic/molecular processes dominate; however, with an increase in beam overlap heat modification becomes more prevalent due to a higher accumulation of energy [16]. Electronic damage is caused by high electron densities which occur due to reflections and refractions.

Far UV wavelength can be used for processing transparent materials. UV radiation allows for linear absorption to be utilized. Specifically, shorter wavelengths can be focused to a smaller spot size, which reduces the thermal damage zone [2]. When considering non-linear phenomena photon wavelength becomes less important, when the same result can be accomplished with laser wavelengths that are more commonly available. Therefore, shorter pulse durations can be utilized which don't require difficult to produce optical components needed for extreme ultraviolet radiation [21].

Long nanosecond laser pulse milling quality is limited by thermal processes: thermal stress, surface micro-cracks, melting, and vaporization [22]. Produced thermal stress results in the generation of glass fractures which in turn increase absorption [6]. The increase appears due to a lower ablation threshold on rougher surfaces [23]. These cracks may allow to have a higher milling rate but may also result in damage in the form of chips or larger cracks which could lead to the destruction of the sample. Using ns is more energy-efficient than with shorter pulses since the debris is small glass pieces formed due to cracking [24]. However, cracking and roughness can be reduced by using shorter picosecond pulses [6]. Since short and ultrashort laser pulses affect the material faster than it can heat up described by two temperature model and in a smaller micro/nanometer area [16], ps pulses mitigate the formation of HAZ [22]. The resulting channels milled with ps pulses were reported to have smoother surfaces, ~8 μm diameter, and depths of 30 μm in FS [1]. Ultrafast pulses can also achieve "cold machining", where the material is removed without the formation of HAZ [7], [22].

Ablation techniques:

Direct laser ablation or top-down technique can be used for milling small glass samples with complicated shapes, coatings, or colorized glasses. The ablation begins at the top of the sample and material is removed layer by layer as it moves down. The produced channel has a V shape, as shown in Figure 1 a), where the angle of the resultant V slope is the taper angle. Channels get such a form because of the scattering and reflections from the channel walls which get their initial angle due to beam shape [16]. The taper angle can be reduced by utilizing a top-hat beam shape. The resulting surface has been reported to have lower roughness compared to the conventional use of a Gaussian beam with little to no reduction in the milling rate [25]. Relatively low heat conductivity of glass causes stress gradient to build up during ablation. This significantly limits the milling rate on thicker samples. In addition, the removed material remains on the sample and can interfere with the laser beam. Plasma shielding is especially significant for shorter laser pulses since the time it takes for electrons to transfer the energy to the lattice is in the range of several ps up to tens of ps. Furthermore, plasma can be expected to disperse on a nanosecond scale [7]. The addition of water as spraying water mist, water jet, or submersion of the workpiece in still or moving water not only removes the debris but also provides cooling, allowing to increase the laser power and therefore milling rate [1], [6].

Alternatively, air blowing at the machining area could be used to remove debris and provide some cooling [1], [2]. However, care needs to be taken to ensure that debris is not blown on the lens or other optics. Water is superior to air due to its higher thermal capacity, but it is more difficult to integrate.

Alternatively, a bottom-up process can be used, where the laser beam goes through the sample and is focused on the bottom side. The debris is removed through the backside which reduces scattering by not obstructing the beam path [6]. Consequently, deeper channels can be formed [8]. The resulting channel sides are parallel to each other since the milling conditions remain constant for each layer being milled, excluding the surfaces (Figure 1 b)). This process is only applicable for glasses with relatively high transmission and good front surface quality [6].

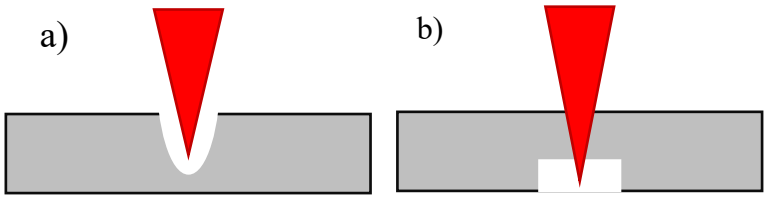

Figure 1. a) top-down and b) bottom-up techniques.

Glass machining techniques:

Glass machining techniques are categorized into four groups: mechanical, thermal (laser), chemical, and hybrid. Some of the techniques belonging to these groups will be introduced here.

Mechanical: For example, mechanical drilling, which inflicts deformation due to thrust resulting in potential cracks. The machined surfaces are rough. However, the process is simple, cost-effective, and could allow for rapid prototyping. It is possible to produce channels with an aspect ratio of 0.33 to 3.96, however, the diameter is limited to 100 µm [1].

Thermal (laser): CO_2 laser is relatively cheap and allows for fast drilling speeds, therefore it is suitable for industrial applications. Material is removed by long (hundreds of nanoseconds [26]) pulses, this results in thermal impact and generation of cracks [1]. To mitigate the negative aspect of crack formation, preheating or heating during the milling of the workpiece can be employed, also, post-treatment of heating the workpiece in an oven. It is possible to achieve surface roughness of several microns *R*a, a hole diameter of 25 µm with an aspect ratio of 4, and a drilling speed of 20000 µm/s per hole [1].

Water-assisted laser ablation reduces the HAZ, temperature gradient, and bulges (which form due to the recast of debris). Convection due to thermal gradient, forced water flow, and formation and collapse of cavitation bubbles aid in the removal of the ablated material from the ablation zone mitigating laser beam shielding [1], [6], [9]. Surface roughness is expected to be lower with water-assisted ablation when in ambient air due to mitigation of debris recast [8]. Additionally, water could be substituted with other liquids. Those that have lower viscosity perform better due to the decreased likelihood of trapping bubbles inside the cavity and therefore more efficient removal of debris [27]. To achieve the highest throughput the laser beam should be focused on the liquid-water interface because if it is more in the liquid the additional vapor produced due to increased heat interferes with the ejection of debris [27]. If

the laser beam is more in the glass the process would eventually terminate due to decreased fluence at the liquid-water interface or produce cracks.

Chemical: Wet etching where the material is submerged in etchant (commonly HF) and areas that are not masked are removed. The process produces round edges due to the amorphous nature of glass, resulting in an aspect ratio lower than 1. Additional stress from the mask or tensile, or compressive stress can result in pinhole and botching defects. Hole diameters of more than 1 μm and surface roughness of down to 30 nm *R*a are achievable. The etching rate can be greatly enhanced by treating glass under femtosecond lasers [1], [22]. Produces no micro-cracks or HAZ. Alternatively, it was shown that creating the acidic solution at the machining area via electrochemical acidification utilizing an electrode can improve the machining speed and would require no masks [1].

Hybrid: Process is defined as multiple processes and mechanisms being used and controlled simultaneously. One of these processes is called spark-assisted chemical engraving (SACE), also known as micro-electrochemical discharge machining (ECDM). Material is submerged in an alkaline solution when an electrode is positioned above the machining area and the other one is dipped into the solution. Material removal takes place as a result of the bombardment of charged particles and the heat generated when bubbles form due to high voltage. The performance of the process depends on tool shape and motion, voltage, electrolyte, and machining gap. The resulting holes have an aspect ratio of >10, *R*a of 0.13 μm, and lower HAZ compared to laser processes. A major limitation is the removal of debris from the machining area [1].

Some of the mentioned techniques and others are summarized in Figure 2 as feed rate (milling rate/throughput) dependence on aspect ratio [1] and in Figure 3 as surface roughness *R*a dependence on aspect ratio. These graphs clearly illustrate laser machining superiority over other techniques in terms of aspect ratio and processing rate; however, surface roughness is not the best. The abbreviations mentioned in Figure 2 and Figure 3 are ASJ – abrasive slurry jet, AJM – abrasive jet micromachining, SACE – spark-assisted chemical engraving, USM – ultrasonic machining, DRIE – deep reactive ion etching.

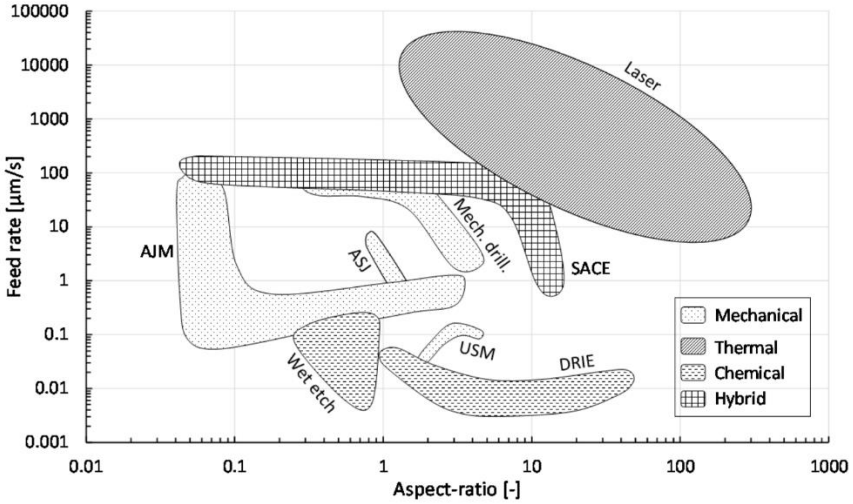

Figure 2. Feed rate (μm/s) dependence on the aspect ratio (μm/μm) for different glass drilling methods, grouped into four categories (mechanical, thermal, chemical, and hybrid) [1].

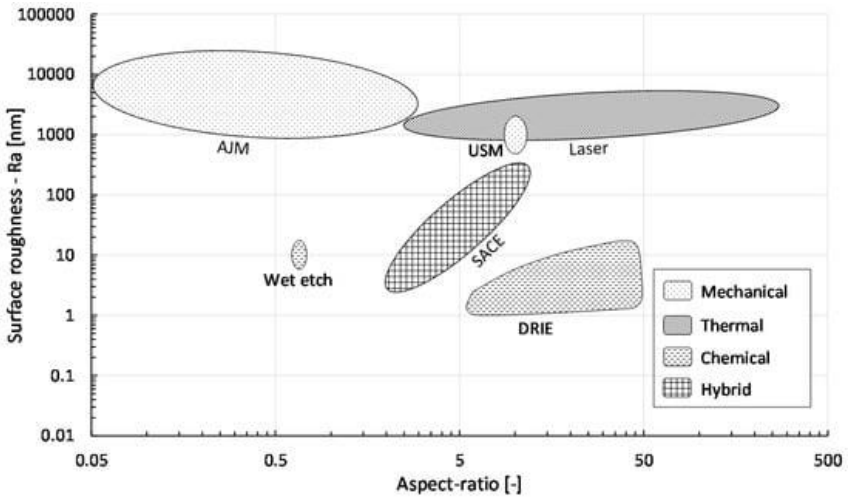

Figure 3. Surface roughness *R*a (nm) dependence on aspect ratio for different glass drilling methods, grouped into four categories (mechanical, thermal, chemical, and hybrid) [1].

Experiment setup:

The experiment was done using an Atlantic 60 (Ekspla) laser which emits 13 ps (at full-width-half-maximum (FWHM) intensity level) pulses at 1064 nm wavelength. The laser provides a 400 kHz pulse repetition rate which was reduced to 50 kHz with a pulse repetition divider. The beam position in the X and Y axes was controlled by an excelliSCAN 14 (ScanLab) galvo scanner, while the sample position in the Z axis was changed with a motorized translation stage 8MT167-100 (Standa). The beam was focused on the workpiece via an 80 mm focal length telecentric f-theta lens. A scheme of the laser setup can be seen in Figure 4. The beam waist radius of 9.5 µm (at $1/e^2$ intensity level) was measured on a chrome-coated glass using the Liu method [28].

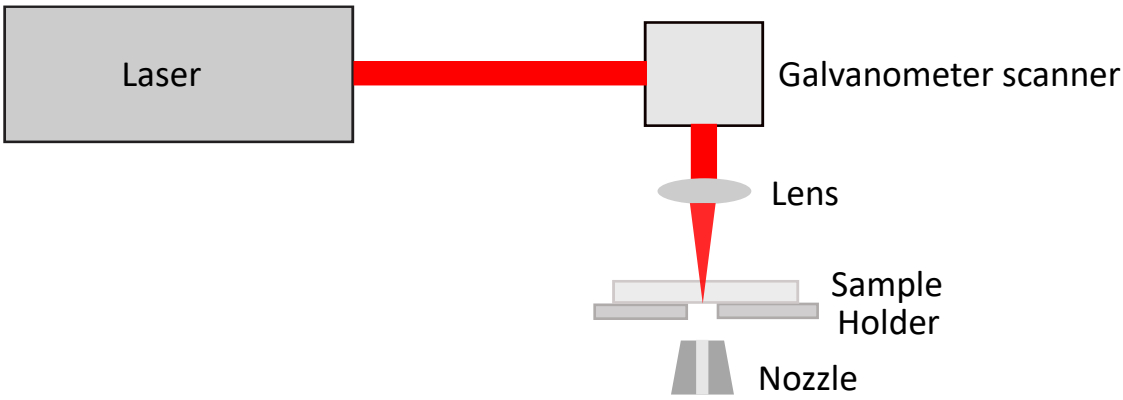

Figure 4. The principal scheme of the experimental setup.

Part of the experiment was done with additional air blowing towards the milling zone. The air was blown from the 2 mm diameter nozzle positioned 5.5 mm below the sample. Two regimes that aided in the removal of dust were used – constant and pulsed air blowing. The pulsed regime was achieved with a directly operated poppet valve VT307 (SMC). The valve opening and closing times were controlled with digital delay and pulse generator Model 565 (BNC). The ablated particles were collected with an AD Oracle iQ (BOFA) vacuum pump working at 150 m^3/h. To collect the dust there must be space under the sample, therefore holders with

holes in them were used (Figure 5). Specialized holders with areas removed where the milling takes place were used. The removed areas are typically as small as possible to direct pressurized air to the milling area (Figure 5 a)). Alternatively, for samples with higher dimensions, a holder with a larger removed area was used (Figure 5 b)). There are other milled areas near the opening that do not go all the way through (grey areas in the figure). They are for milling specialized elements and do not have any influence in our case.

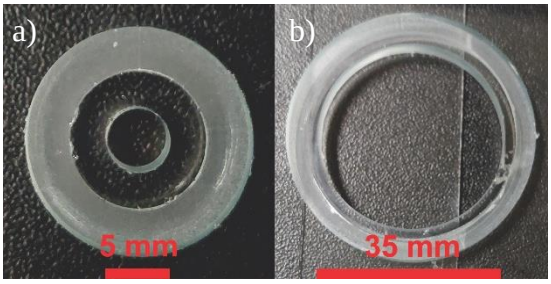

Figure 5. Holders used for the milling of the channels a) with 5 mm diameter hole or milling the objects which fall out of the sample b) with 35 mm diameter hole.

For milling with water-assisted debris removal, the holder and the sample were placed inside a large petri dish with high enough walls to allow the sample to be mostly submerged in water. The holder sample had an outer diameter of 34.2 mm, an inner diameter of 16.5 mm, and a thickness of 4.8 mm. The sample was placed on the holder in a way that the milling area would be inside the inner holder area, but the sample would not fully overlap with the inner holder area. The whole setup was submerged underwater up to 4.3 mm of the milling sample height. This setup is depicted in Figure 6.

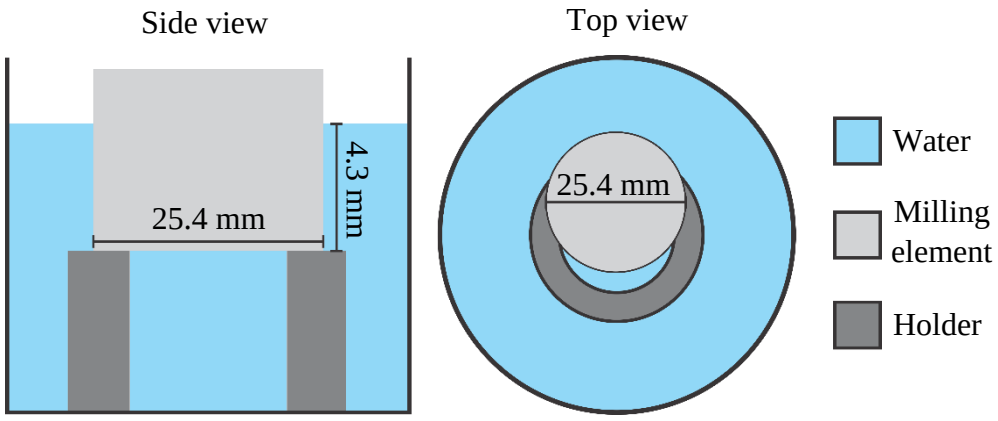

Figure 6. A drawing of the milling setup when the sample was partially submerged in water.

Method:

The focal position was measured by forming craters at different Z positions on a soda lime sample coated with chromium film and then observing the height at which crater diameters were the smallest. The focal position at the bottom surface of the FS sample was recalculated by adding the chromium-coated sample thickness and then subtracting FS sample thicknesses difference by its optical thickness. Laser milling was performed by focusing the beam 100 – 200 µm below the bottom of the sample as in other cases milling was unstable or caused cracks.

The laser beam was scanned in a spiral trajectory, moving inward and outward, and scanning the perimeter once. After every loop, the spiral was rotated by 33° degrees. Rotation was used to ensure that the spiral lines would cover the entire area more evenly. Figure 7 displays the scanned area of a spiral, where the distance between the spiral lines is denoted as spacing and the distance between laser shots in the line as pitch. The sample was moved downwards by distance *dz* vertically after every loop. Beam scanning in the X and Y axis and moving in the Z axis was repeated until the channel was formed.

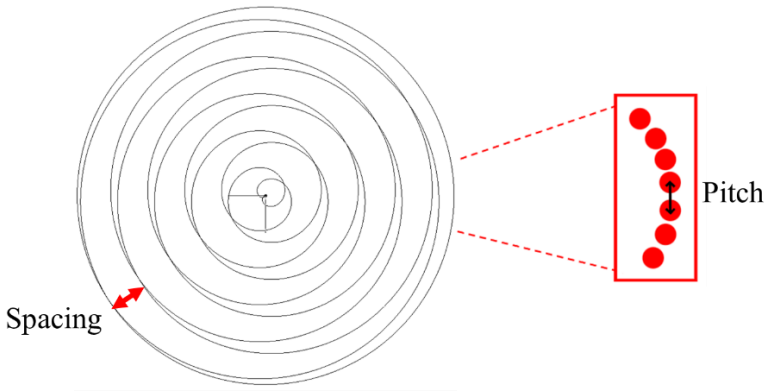

Figure 7. Laser scanning trajectory used for channel formation.

A 152 mm x 152 mm x 6.3 mm FS sample was used for most of the experiment and for investigation of minimal diameter an additional 1 mm thickness and 100 mm diameter FS sample was used.

The milling rate of the channels was calculated using formula (8), where v is the milling rate, r is the channel radius, t is the milling time, and h is the depth of the channel. Milling duration was acquired by taking the real time it took to mill the channel. Therefore, jumps between scanning lines, and extra loops before and after the milling were included. Channels with the highest milling rate were considered to have optimal parameters.

$$v = \frac{milled\ volume}{milling\ time} = \frac{\pi r^2 h}{t} \tag{8}$$

Milling efficiency was calculated using formula (9), here P is average power, E is pulse energy, and f is pulse repetition rate.

$$\eta = \frac{milled\ volume}{total\ energy} = \frac{\pi r^2 h}{tP} = \frac{\pi r^2 h}{tEf} \tag{9}$$

The experiment was divided into five parts:

Part 1: finding optimal pitch and spacing.

The experiment started with finding the optimal pitch and spacing values for the pulse energy of 63 µJ. The pitch was changed from 1 µm to 5 µm every 1 µm. For each pitch value, the spacing values were changed in the range of 8 µm to 30 µm. For every different pitch and spacing combination, the *dz* value was changed until the highest value with which the stable milling of the channel could be achieved (explained in Figure 9). It was chosen to mill 1 mm diameter channels as the ablated parts could be removed without getting stuck. To save time, the channel height was 2 mm which was smaller than the sample thickness. In this part, regimes with continuous airflow at 0.1 MPa pressure, without additional airflow, and when the sample was submerged in distilled water were investigated.

Part 2: finding the optimal pulse energy.
The optimal pitch and spacing values were taken from the first part, and the investigation into the pulse energy that would result in the highest milling rate was carried out. The pulse energy was changed from 10 μJ to 90 μJ every 10 μJ. For each pulse energy value, the spacing value was changed in the range of 8 μm to 30 μm. For every different pitch and spacing combination, the *dz* value was changed until the highest value with which the stable milling of the channel could be achieved. It was chosen to mill a 1 mm diameter and 2 mm depth channel. In this part, only continuous airflow at 0.1 MPa pressure was used.

Part 3: investigating airflow parameters.
Continuous airflow pressure was investigated by observing the milled depth of the channel changing pressure from 0 MPa to 0.7 MPa every 0.1 MPa. Also, the duration for which the pulsed airflow valve was opened and closed was changed. The opening time was changed from 100 ms to 700 ms by a step of 100 ms for every closing time of 50 ms, 100 ms, and 150 ms.

Part 4: searching for the minimal diameter.
A search for the smallest possible channel diameter was conducted with the optimal pitch and pulse energy values determined in the previous sections. Milling was done on a 6.3 mm thickness FS sample with continuous, pulsed, without additional airflow, and when the sample was submerged in distilled water. Also, a 1 mm FS sample was milled with the method which produced the smallest diameter. For this, full-depth channels were milled. The diameter was changed from 1.6 mm to the lowest possible by a step of 0.2 mm. The step was lowered when the minimal diameter was reached or when it became larger than the diameter. Then *dz* was changed until the highest value with which the stable milling of the channel could be achieved. Additionally, samples were cut in half to acquire the surface roughness as described in the sample characterization part. Channel roughness was compared when they were milled with different diameters using continuous airflow towards the milling area.

Part 5: milling a channel with an angle.
Channels were milled with an angle (Figure 8) by adding an offset to the scanned area for each loop. The highest angle was noted for comparison when milling was done with continuous and pulsed airflow, and when the sample was partially submerged in still distilled water. The channels were milled with 1 mm diameter, 70 μJ pulse energy, and for the full 6.3 mm depth.

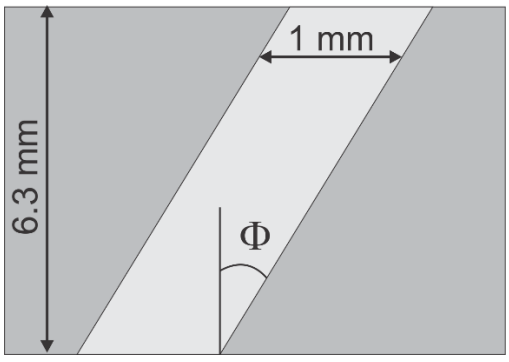

Figure 8. Drawing of a channel milled with an angle Φ.

Sample characterization:

To determine if the channel was acceptable a visual inspection was carried out. While milling, it was noticed that the plasma sometimes would have irregularities, such as brighter or darker spots, or deviations from the perfect circle. When the mentioned irregularities were observed milling would be stopped because it would fail if they persisted for a few seconds. Such channels would have fused dust in them, which couldn't be removed with pressurized air, or cracks. Even if the milling was stopped shortly after the irregularities were noticed, the channel would still have defects.

After the milling, channels were blown with pressurized air to remove any dust left from the milling process. Then the channels were inspected by eye or by microscope if it was difficult to inspect with an eye. Channels that had cracks or visible fused dust were considered to have failed. However, small cracks and a low amount of debris were accepted. Examples of failed a-b) and acceptable c-d) channels are displayed in Figure 9.

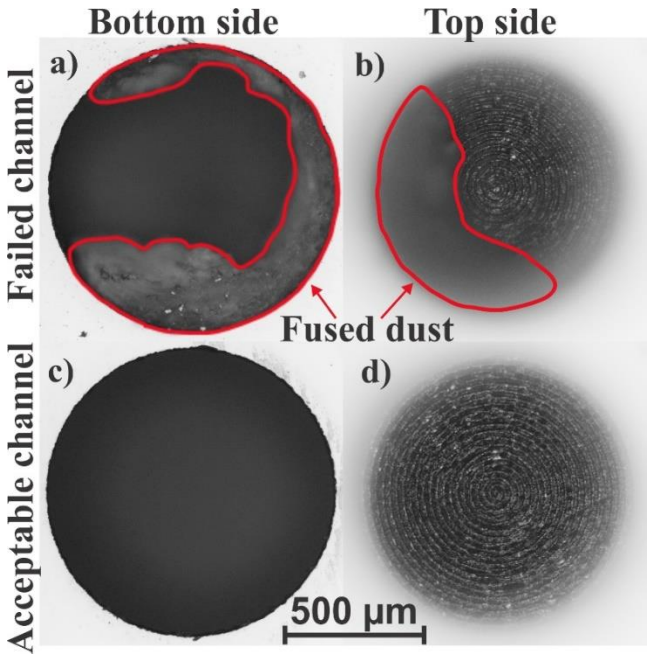

Figure 9. The microscope images of channels bottom (a, c) and top (b, d) sides. A failed channel with fused dust is shown at the top of the figure and an acceptable channel is shown at the bottom of the figure.

For the surface roughness measurements, a channel was milled with a rectangle around it as shown in Figure 10 a), where the red area was milled. For this purpose, a different holder was used so that the product would not get sucked into the pump which collects the glass dust (Figure 5 b)). The surface roughness was measured with an optical profilometer (S Neox, Sensofar) utilizing the confocal regime. To categorize roughness, parameters like arithmetical mean deviation *R*a, and maximum height of the profile *R*z were used, which come from ISO 4287 standard [29] and were obtained from the SensoVIEW program. To acquire the parameters a line was selected from the surface profile of the channel (Figure 10 b)). 5 measurements were done on each sample varying the placement of the line for surface topography (Figure 10 b)) by a random amount but staying near the lowest depth. The minimal length requirement of 4 mm with a standard cut-off λ_c filter was met as required by ISO 4287 standard for the *R*a values ranging between 0.1 µm and 2 µm [29].

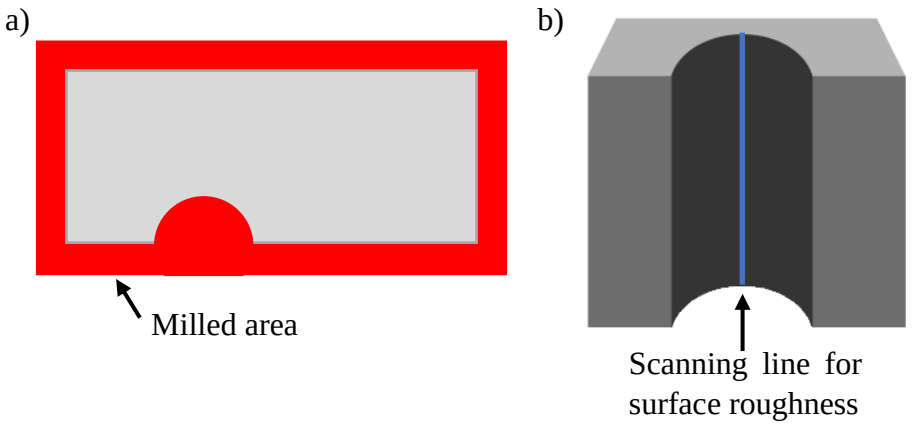

Figure 10. Top a) and side b) view of a rectangle cut around the channel with the channel positioned at the edge and cut in half.

Results and discussion:

Part 1. Finding the optimal pitch.

The optimal spacing dependence on the pitch, when milling with continuous airflow, is shown in Figure 11 a). Optimal spacing values decreased as higher pitch values were used. This could be because for optimal milling parameters spacing had to be reduced so that energy per volume would not change so drastically.

The milling rate and efficiency dependencies for pitch with optimal spacing values are shown in Figure 11 b). It can be seen that the highest milling rate of 1.43 mm^3/min and efficiency of 7.5 μm^3/µJ were achieved using 2 µm pitch, 24 µm spacing, 16 µm *dz*, and 63 µJ pulse energy.

Without constant spacing the dependence is unclear, might be because local peaks were hit. Since not all spacing values were evaluated due to time constraints, global maxima might not have been found.

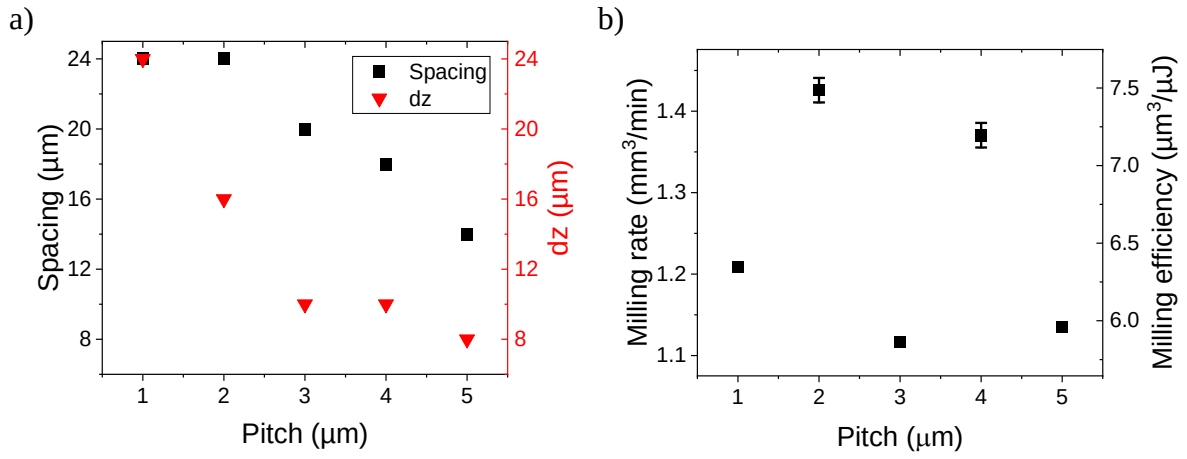

Figure 11. Optimal spacing and *dz* value dependence on pitch a) and milling rate and milling efficiency dependence on pitch b). Milled with continuous airflow and pulse energy of 63 µJ.

An optimal spacing value with water-assisted milling was investigated. A pitch value of 2 µm was chosen as the starting point. The optimal spacing was 16 µm with the highest milling rate of 1.57 mm^3/min and efficiency of 7.52 μm^3/µJ. It was not possible to produce a clean channel with spacing outside of the [10; 18] µm range (Figure 12).

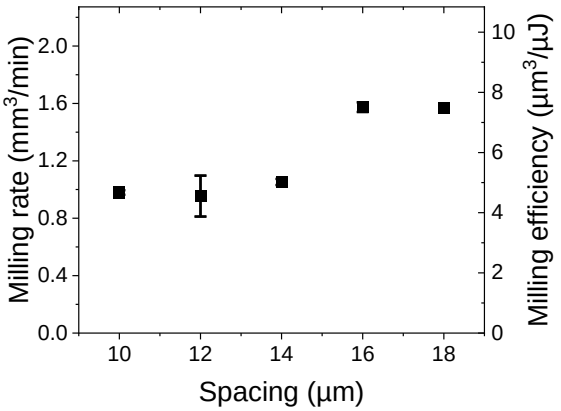

Figure 12. Milling rate and milling efficiency dependence on spacing. The channels were milled in still water with 70 µJ pulse energy and 2 µm pitch.

Pitch optimization was carried out after finding the optimal spacing values. The milling rate and efficiency dependencies on pitch with optimal spacing values are shown in Figure 13, when milling was done without additional debris removal, with continuous airflow at 0.1 MPa pressure, and when the sample was partially submerged in still distilled water. Spacing and pulsed energy values for each debris removal method are written in Table 1.

Table 1. Constant milling parameters for different debris removal methods.

	No additional debris removal	Continuous airflow	Water-assisted
Pulse energy, µJ	63	70	70
Spacing, µm	24	24	16

The highest milling rate of 2.1 mm^3/min and efficiency of 10 μm^3/µJ were achieved with 3 µm pitch, 16 µm spacing, 22 µm *dz*, 70 µJ pulse energy, and water assisted-milling. When compared to water-assisted milling the highest milling rate was 2 and 1.4 times lower with no additional debris removal and continuous airflow, respectively.

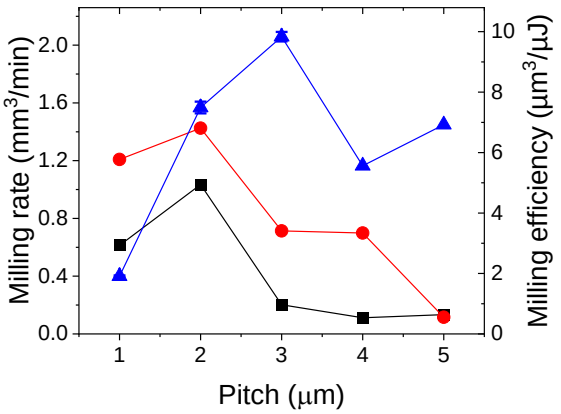

Figure 13. Milling rate and efficiency dependencies on the pitch without additional debris removal, with continuous airflow, and when the sample was partially submerged in still distilled water.

When the spacing was constant there was only one peak with continuous airflow. Supporting the fact that different spacing values produce local peaks. However, without checking a wider range of values it is not possible to determine if the maximum was found or not.

From Figure 13, an optimal pitch of 2 μm and 3 μm for continuous airflow and water-assisted regimes, respectively, were acquired. The pitch was chosen to be constant while spacing was changed to acquire optimal parameters. Since the pitch value was smaller, and with values outside the 1 to 5 μm range no stable regime was found, its change would have had more influence than a small change of spacing.

Part 2. Investigating pulse energy.

The next part of the experiment was done using continuous airflow with the optimal parameters found in the 1st part. Therefore, the channels were milled using 2 μm pitch and 24 μm spacing values. However, for pulse energies below 40 μJ, as shown in Figure 14, stable milling could not be achieved with a 24 μm spacing. Consequently, it becomes necessary to decrease the spacing to introduce more energy per layer. Therefore, for lower pulse energies smaller spacing value of 12 μm was used.

The highest pulse energy of 90 μJ was limited by the laser and the lowest pulse energy was 15 μJ. With lower pulse energy no stable milling could be achieved. The milling rate dependence on pulse energy is shown in Figure 14 a). There were two peaks at 20 μJ and 70 μJ which were observed because they had different spacing values. The resulting milling rates for 20 μJ and 70 μJ pulse energies were 1.2 mm^3/min and 2.1 mm^3/min, respectively. This means it was possible to reach the same milling rate as with water-assisted milling when the pulse energy was increased from 63 μJ to 70 μJ.

It was not possible to increase the milling rate via an increase in the pulse repetition rate due to galvanometer scanner speed limitations. For this reason, further experiments were conducted with 70 μJ pulse energy which produced the highest milling rate.

The milling rate was increasing with an increase in pulse energy up to 70 μJ after which it started to decrease rapidly. This could be because with higher pulse energy electrons get superheated at the glass-air interface. After that, electrons are ejected and ionize the ambient air into plasma which in turn disrupts the expansion of the ablated material, resulting in lower milling efficiency [8].

The milling efficiency dependence on pulse energy is shown in Figure 14 b). It can be seen that milling efficiency tended to decrease as higher pulse energy was used. Therefore, the highest efficiency of about 20 μm^3/μJ was achieved with a pulse energy of 15 μJ. However, the milling rate was about 2 times lower compared to the highest at 70 μJ pulse energy. A 2 times lower milling efficiency of 10 μm^3/μJ was achieved with 70 μJ pulse energy.

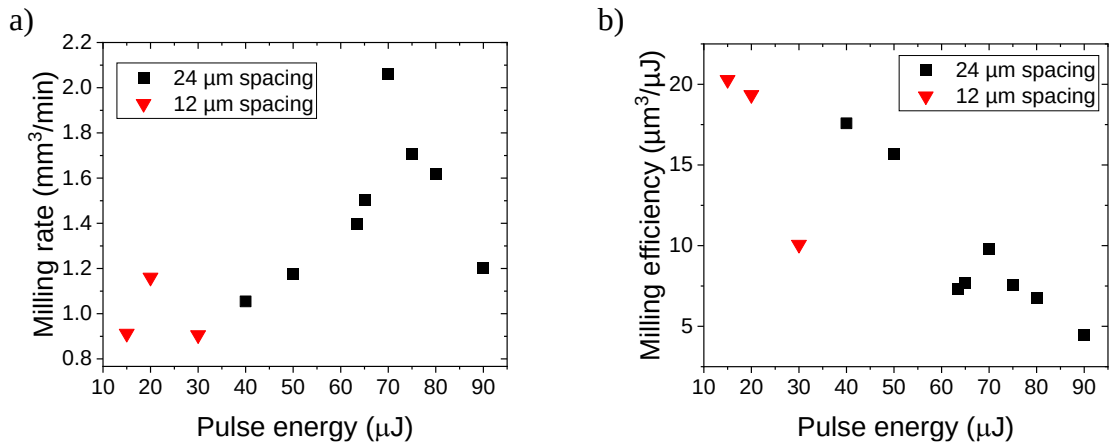

Figure 14. Milling rate dependence on pulse energy a) and milling efficiency dependence on pulse energy b).

The optical pictures of channels milled with different pulse energies are shown in Figure 15. Picture c) does not have clear spiral lines as seen in a) at the end of the milling. Both channels were repeated three times without failure, indicating that clear spiral lines are not necessary, and a small amount of dust is not detrimental to the channel. Even for the channels which were heavily dusted or cracked spiral lines were often observed. Therefore, they cannot be relied upon to determine if the channel is acceptable.

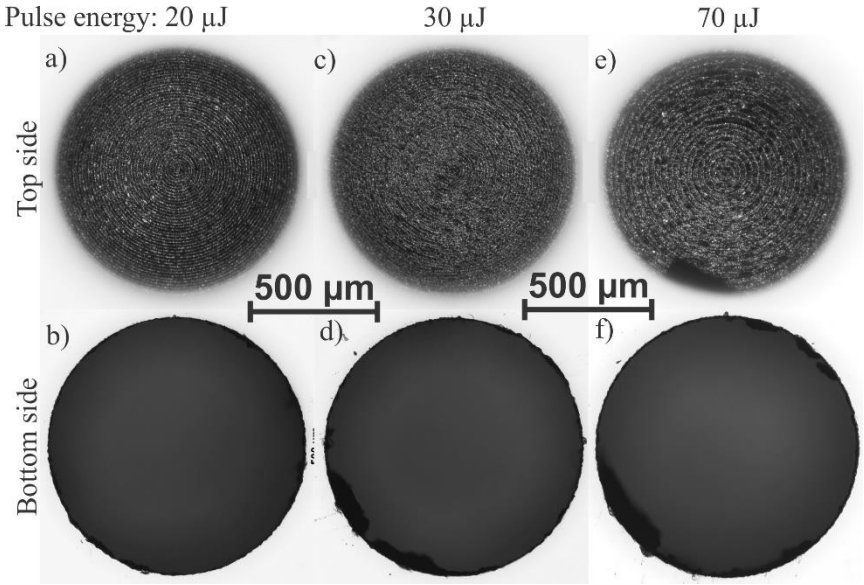

Figure 15. Microscope photos of channels formed with different pulse energies a-b) 20 µJ, c-d) 30 µJ, e-f) 70 µJ. The spacing was set to 12 µm for a-d) and 24 µm for e-f).

Part 3. Investigating airflow parameters.

To achieve full-depth channels with higher milling rates and efficiencies the pressure was changed for continuous airflow and the time for which airflow was open and closed with pulsed regime. For this purpose, a channel that cracked before reaching the full depth was milled. It was selected so that the milled depth with different regimes could be compared. The milling parameters were: 0.2 mm diameter, 24 µm spacing, 1 µm *dz*, and 70 µJ pulse energy on a 6.3 mm FS sample.

Figure 16 a) shows that for the mentioned parameters higher pressure allowed forming deeper channels. After 0.3 MPa pressure was reached, the milled depth saturated to about 4.5 mm. However, a higher 0.6 MPa pressure was selected for pulsed airflow and further experiments because it resulted in a slightly higher milled depth. Even higher pressure was not available due to system limitations.

As seen in Figure 16 a) it was possible to form deeper channels when airflow was open for a longer time, in other words, as it approached continuous airflow.

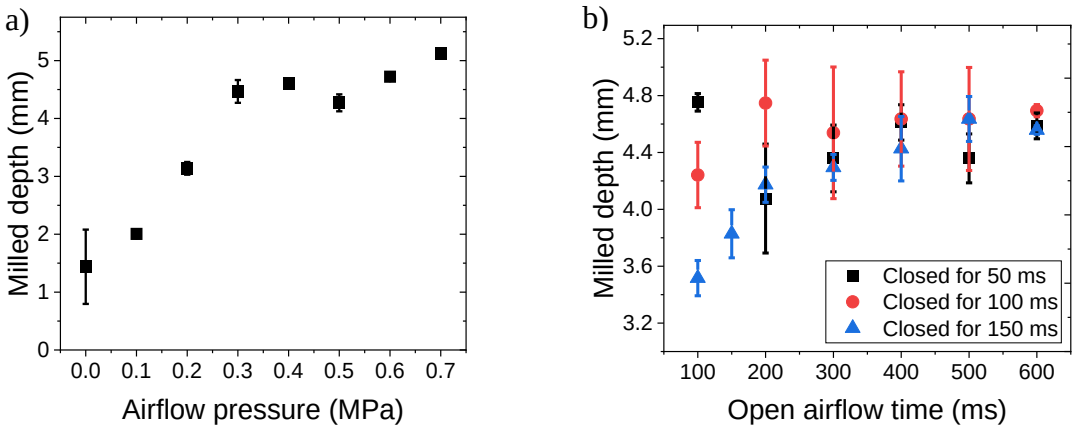

Figure 16. With continuous airflow milling depth dependence on airflow pressure a) and on closed and opened time of the valve b) with pulsed airflow at 0.6 MPa pressure. Error bars are standard deviation calculated from 3 millings.

Part 4. Finding the minimal achievable diameter.

Milling without additional debris removal.

It was not possible to mill the whole 6.3 mm depth and the maximum achieved depth was about 2.3 mm, for channel diameters ranging between 0.2 mm – 1.6 mm.

The top sides of the channels were heavily dusted, but spiral lines were observable with dark-field microscopy as seen in Figure 17. This further supports the fact that spiral lines are not indicative of good channel quality. However, the bottom sides of the channels were mostly clean.

Since it was impossible to mill full-depth channels, diameter dependence on milling rate and efficiency cannot be adequately compared to the ones done with additional debris removal methods.

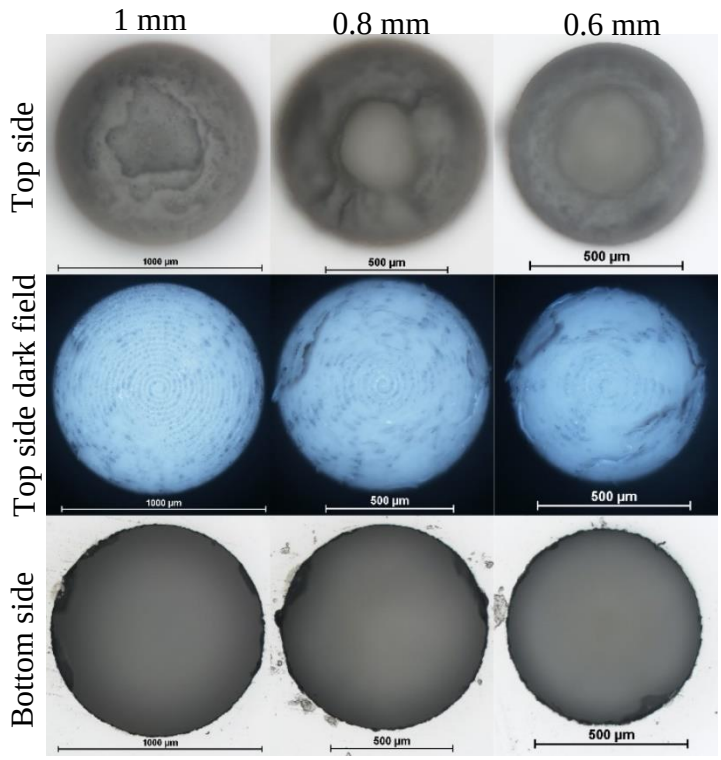

Figure 17. Microscope images of channels that failed before full depth was milled.

Milling with additional debris removal methods:

The smallest diameter of 300 µm was milled with continuous airflow, as seen in Figure 18 and Figure 19 b). The 300 µm diameter channel was milled with 14 µm *dz*, a milling rate of 1 mm^3/min, and a milling efficiency of 4.7 $µm^3$/µJ. This resulted in the highest aspect ratio of 21. At first, decreasing the diameter allowed for a higher milling rate, but after reaching 600 µm diameter it started to decrease. For lower diameters accumulation phenomena might have started to add up which would cause the milling to fail. Lowering *dz* could result in the laser beam becoming out of focus lowering the fluence and allowing for stable milling.

When milling with pulsed airflow, the valve was closed and open for 150 ms. For 1 to 1.4 mm diameters the milling rate and efficiency were about 15% higher with pulsed airflow than with continuous airflow, for other diameters, it was about 20% lower (Figure 18). The smallest achieved diameter was 800 µm.

The smallest diameter achieved with still water was 600 µm which also had the highest milling rate of 1.45 mm^3/min and efficiency of 6.9 $µm^3$/µJ (Figure 18). There was a general trend of increasing milling rate and efficiency with decreasing diameter. Only the 1 mm diameter differed, for it to achieve stable milling *dz* had to be lowered from 22 µm, used in pitch optimization, to 8 µm. Otherwise, cracks would form soon after the milling started. The milling rate and efficiency were on average 2.5 times lower when milling with the sample partially submerged in water than with continuous airflow.

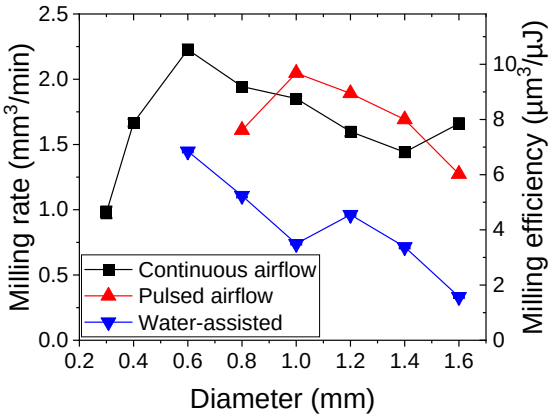

Figure 18. Milling rate and efficiency dependence on diameter with additional debris removal methods.

Channels milled with pulse airflow had more fused dust on the bottom compared to when the channel was milled with continuous airflow (Figure 19). The channel with a 600 µm diameter did not crack but was full of fused dust and appeared dark when observed with an optical microscope using bottom illumination. The larger diameter channels had fewer defects.

Continuous airflow and water-assisted milling produced the overall cleanest channels. The chipping sizes were smaller than 60 µm. However, when milling in still water there was more fused dust at the top side edges of the channel. This possibly occurred due to water not being able to reach the milling area in time.

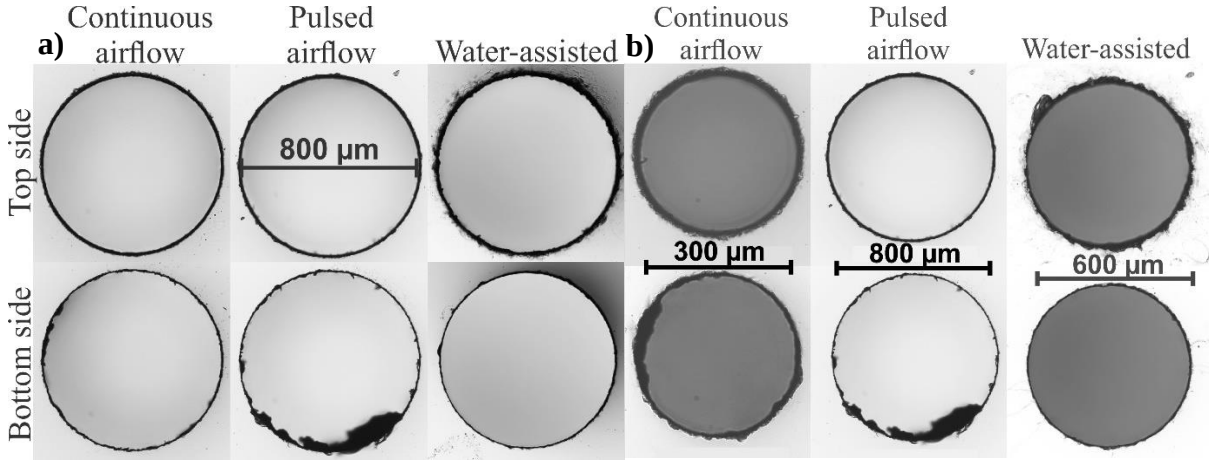

Figure 19. Microscope pictures of 800 µm diameter channels a) and with smallest achieved diameters b) milled with different debris removal methods.

Milling with continuous airflow on 1 mm thickness fused silica:

The smallest diameter was produced with continuous airflow, therefore, to see if it can be further reduced milling on a 1 mm FS sample was carried out. The airflow pressure was reduced from 0.6 MPa to 0.4 MPa to avoid breaking the thin sample.

The fastest milling time of 3 seconds on the thin sample was reached with a 200 µm diameter (Figure 20 b)). After which *dz* had to be reduced from 14 µm to 4 µm and was further divided by 2 for lower diameters (Figure 20 d)). The smallest diameter achieved on a 1 mm thickness FS sample was 40 µm with 0.5 µm *dz*, milling rate of 3.1×10^{-3} mm^3/min, milling efficiency of 14.96×10^{-3} µm^3/µJ, and milling time of 24 s (Figure 20). This resulted in a higher aspect ratio of 25.

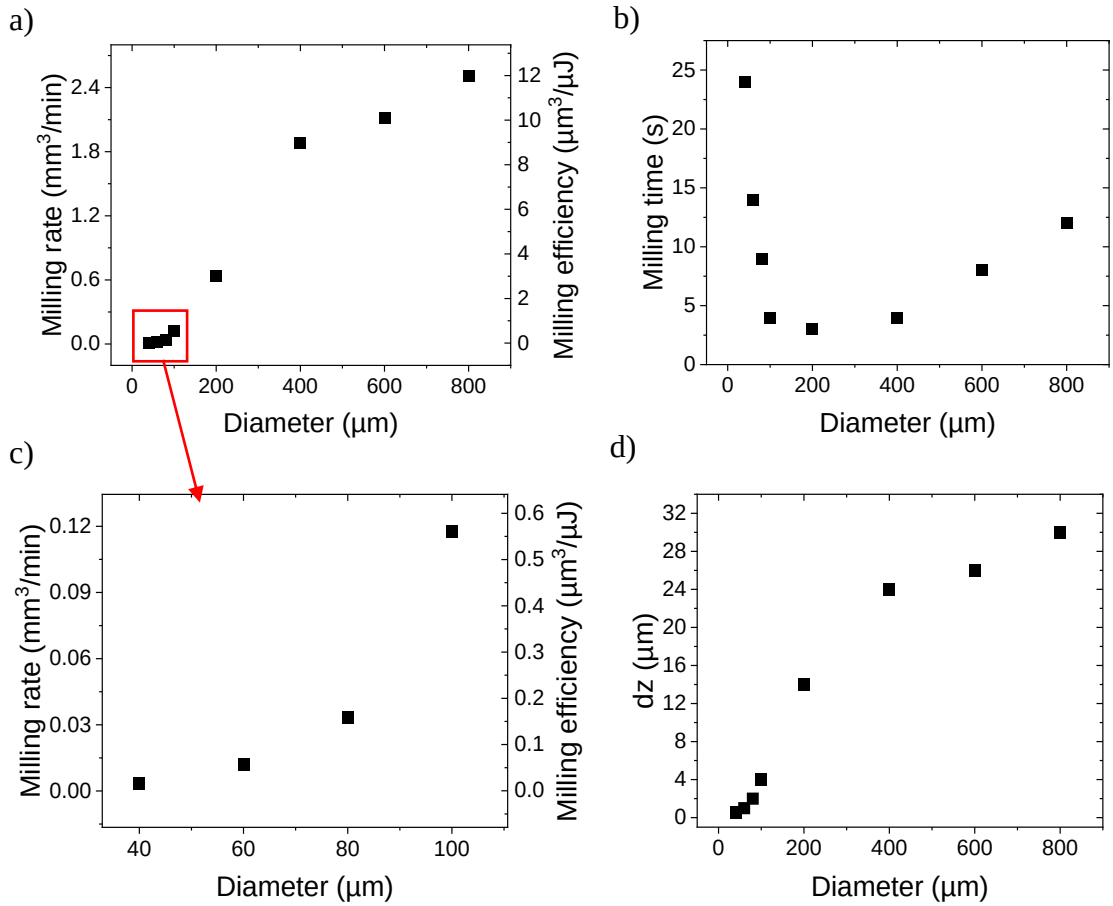

Figure 20. Milling rate a), milling time b), milling efficiency c), and *dz* d) dependencies on channel diameter. Channels were milled on 1 mm thickness FS with continuous airflow.

Figure 21 features channels milled on 1 mm thickness FS glass. As the diameter was lowered the areas with fused dust in the channels increased. It was especially apparent with diameters lower than 100 µm. In addition, the bottom and top sides of the channels became more irregular, which possibly came from high spacing (24 µm) value. Considering that the beam waist was 10 µm, spiral scanning might not be able to form a circular with higher spacing values.

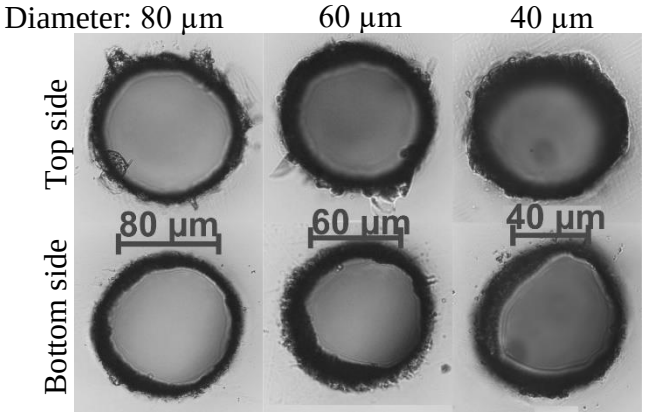

Figure 21. Pictures of channels with smallest diameters milled on 1 mm thickness FS with continuous airflow.

Surface roughness:

The channels' sidewall roughness dependence on channel diameters was investigated. For this purpose, channels were cut in half and the channel topography was scanned with the optical profilometer. An example of a channel surface topography is displayed in Figure 22.

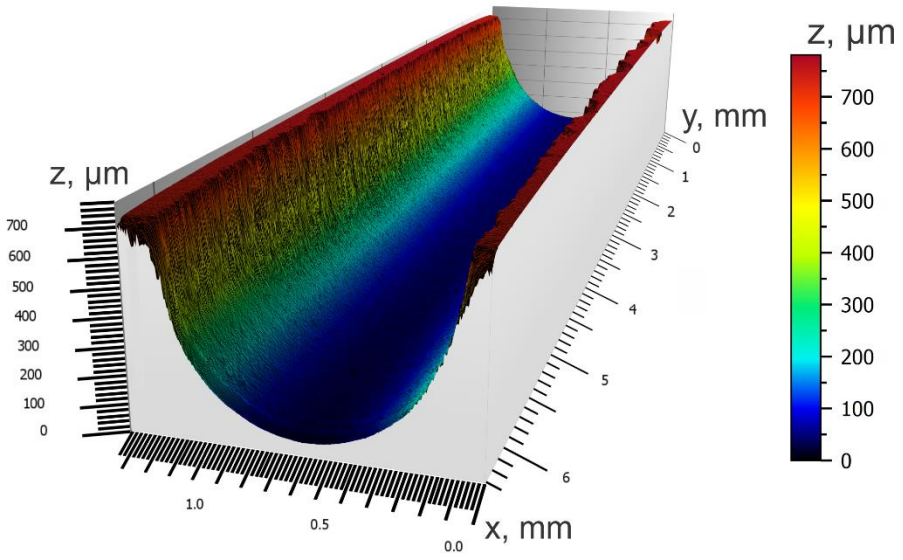

Figure 22. Surface topography of a 1.2 mm diameter channel.

Surface roughness was measured for different diameter channels milled with continuous airflow (Figure 23). The milling parameters were the same as in Figure 18. The regime of continuous airflow was selected as it allowed the formation of the smallest diameter channels. It appears that as the diameter decreases, roughness tends to increase. The increase in roughness likely originated due to the accumulation of debris at the channel walls as seen with lower diameter channels in Figure 19 and Figure 21. The range of *R*a for all diameters was [0.68; 1.21] µm and the *R*z was [5.7; 11.2] µm.

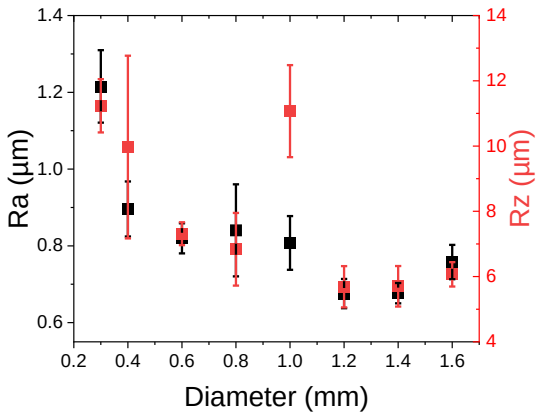

Figure 23. Surface roughness parameters *R*a and *R*z dependence on diameter. Error lines are the standard deviation of 5 measurements from the same sample.

Part 5. Milling with an angle.

Using the same parameters as when milling full 6.3 mm depth 1 mm diameter channels in FS, channels with the highest possible angle were milled. With continuous airflow the highest angle was 14 degrees, with pulsed airflow it was 15 degrees, and with still water, it was 24 degrees. Increasing the angle by just 1 degree resulted in the channel cracking midway or towards the end of the milling.

The top sides of the channels became a bit elliptic as seen in Figure 24. The ellipticity likely occurred due to the process not terminating immediately after reaching the top, resulting in some direct ablation only on one side.

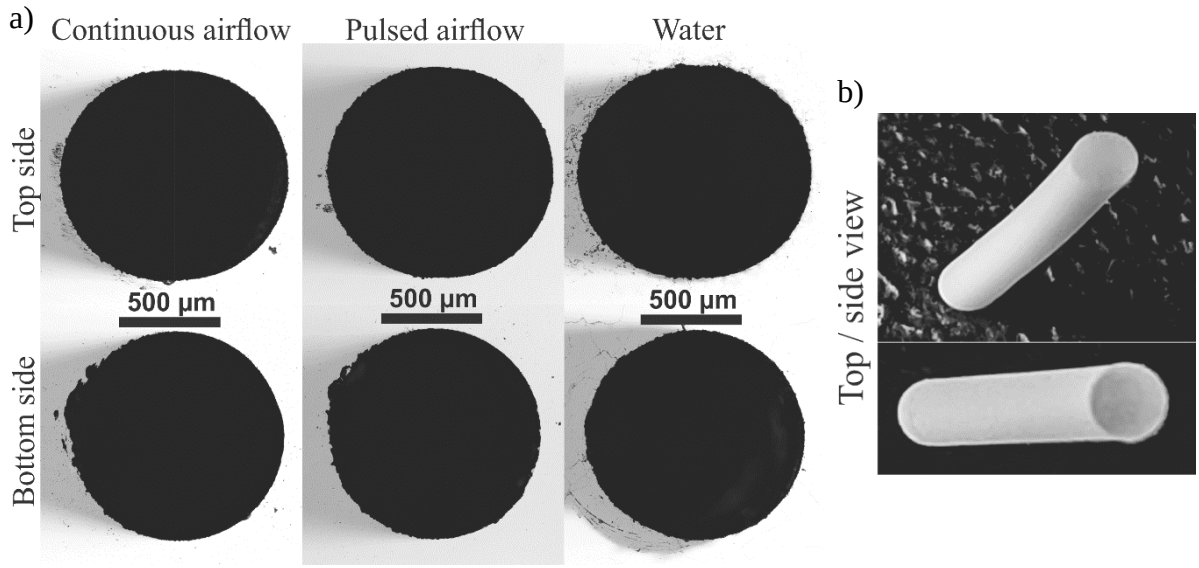

Figure 24. Microscope pictures of the top and bottom sides of channels that were milled with the highest angles and different debris removal methods a) and photos of the channel with the highest angle b).

Main results and conclusions:

1. It is crucial to remove the debris from the laser interaction zone because it enhances the milling process allowing for the formation of deeper channels with improved milling rate.
2. To achieve the smallest diameter in 6.3 mm fused silica, continuous airflow needs to be utilized. The smallest channel' diameter of 300 μm giving an aspect ratio of 21 was formed, while with other debris removal methods, the smallest diameter was twice or more as big.
3. Diameters smaller than 100 μm were formed when milling in 1 mm fused silica with continuous airflow.
4. Water is needed to form a channel with the steepest angle when milling a 1 mm diameter and 6.3 mm depth channel. Water-assisted milling allowed the formation of a channel with a 24-degree angle, while airflow resulted in 14-15 degrees.

References:

[1] L. A. Hof, J. A. Ziki, H. Jiang et al., Micro-Hole Drilling on Glass Substrates—A Review, *Micromachines (Basel)*, p. 53, Feb. 2017, doi: 10.3390/MI8020053.

[2] S. Nikumb, Q. Chen, C. Li et al., Precision glass machining, drilling and profile cutting by short pulse lasers, *Thin Solid Films*, pp. 216–211, Apr. 2005, doi: 10.1016/J.TSF.2004.08.136.

[3] J. Dudutis, G. Račiukaitis, P. Gečys et al., High-density gas capillary nozzles manufactured by hybrid 3D laser machining technique from fused silica, *Opt. Express*, pp. 27965–27977, Oct. 2018, doi: 10.1364/OE.26.027965.

[4] R. L. Sutherland, D. G. Mclean, and S. Kirkpatrick, *Handbook of Nonlinear Optics*, Second Edition. New York: Marcel Dekker, 2003. doi: 10.1201/9780203912539.

[5] Products Catalogue — Ekspla. https://ekspla.com/products/#new_tab (accessed Jan. 07, 2024).

[6] J. Dudutis, G. Račiukaitis, E. Daknys et al., Quality and flexural strength of laser-cut glass: classical top-down ablation versus water-assisted and bottom-up machining, *Opt. Express*, pp. 4564–4582, Jan. 2022, doi: 10.1364/OE.447143.

[7] A. Tuennermann, S. Nolte, and J. Limpert, Femtosecond vs. Picosecond Laser Material Processing, *Laser Technik Journal*, pp. 34–38, Jan. 2010, doi: 10.1002/LATJ.201090006.

[8] X. Zhao and Y. C. Shin, Femtosecond laser drilling of high-aspect ratio microchannels in glass, *Appl Phys A Mater Sci Process*, pp. 713–719, Aug. 2011, doi: 10.1007/S00339-011-6326-Z/METRICS.

[9] W. Charee and V. Tangwarodomnukun, Dynamic features of bubble induced by a nanosecond pulse laser in still and flowing water, *Opt. Laser Technol.*, pp. 230–243, Mar. 2018, doi: 10.1016/J.OPTLASTEC.2017.10.019.

[10] Absorption. https://www.rp-photonics.com/absorption.html (accessed Jul. 13, 2023).

[11] K. Obata, K. Sugioka, T. Akane et al., Efficient refractive-index modification of fused silica by a resonance-photoionization-like process using F(2) and KrF excimer lasers, *Opt. Lett.*, p. 330, Mar. 2002, doi: 10.1364/OL.27.000330.

[12] Materials Data - Fused Silica / Fused Quartz | Esco Optics – Esco Optics, Inc. https://escooptics.com/pages/materials-fused-silica-quartz (accessed Aug. 01, 2023).

[13] A. M. Efimov and V. G. Pogareva, IR absorption spectra of vitreous silica and silicate glasses: The nature of bands in the 1300 to 5000 cm− 1 region, *Chem. Geol.*, pp. 198–217, May 2006, doi: 10.1016/J.CHEMGEO.2006.01.022.

[14] Audrius Dubietis, *Netiesinė optika*. Vilnius university, 2011.

[15] I. N. Zavestovskaya, P. G. Eliseev, O. N. Krokhin et al., Analysis of the nonlinear absorption mechanisms in ablation of transparent materials by high-intensity and ultrashort laser pulses, *Appl. Phys. A.*, pp. 903–906, Sep. 2008, doi: 10.1007/S00339-008-4609-9.

[16] M. Sun, U. Eppelt, C. Hartmann et al., Numerical analysis of laser ablation and damage in glass with multiple picosecond laser pulses, *Opt. Express*, pp. 7858–7867, Apr. 2013, doi: 10.1364/OE.21.007858.

[17] M. Ams, D. J. Little, and M. J. Withford, Femtosecond-laser-induced refractive index modifications for photonic device processing, in *Laser Growth and Processing of Photonic Devices*, N. A. Vainos, Ed., in Woodhead Publishing Series in Electronic and Optical Materials. Woodhead Publishing, 2012, pp. 305–332. doi: 10.1533/9780857096227.3.305.

[18] M. Sun, U. Eppelt, S. Russ et al., Laser ablation mechanism of transparent dielectrics with picosecond laser pulses, *Laser-Induced Damage in Optical Materials: 2012*, pp. 41–50, Dec. 2012, doi: 10.1117/12.976062.

[19] C. Byram, S. Satya, B. Moram et al., Modelling ultrafast laser ablation, *J Phys D Appl Phys*, p. 193001, 2017, doi: 10.1088/1361-6463/50/19/193001.

[20] J. Shin and K. Nam, Groove Formation in Glass Substrate by a UV Nanosecond Laser, *Appl. Sci.*, p. 987, Feb. 2020, doi: 10.3390/APP10030987.

[21] J. Meijer, K. Du, A. Gillner et al., Laser Machining by short and ultrashort pulses, state of the art and new opportunities in the age of the photons, *CIRP Annals*, pp. 531–550, Jan. 2002, doi: 10.1016/S0007-8506(07)61699-0.

[22] X. Z. Xie, C. X. Zhou, X. Wei et al., Laser machining of transparent brittle materials: from machining strategies to applications, *Opto-electron. adv.*, p. 180017, 2019, doi: 10.29026/OEA.2019.180017.

[23] K. Nagayama, Y. Kotsuka, T. Kajiwara et al., Pulse laser ablation of ground glass, *Shock Waves*, pp. 171–183, Nov. 2007, doi: 10.1007/S00193-007-0103-0/METRICS.

[24] J. Dudutis, J. Pipiras, R. Stonys et al., In-depth comparison of conventional glass cutting technologies with laser-based methods by volumetric scribing using Bessel beam and rear-side machining, *Opt. Express*, pp. 32133–32151, Oct. 2020, doi: 10.1364/OE.402567.

[25] H. Le, P. Penchev, A. Henrottin et al., Effects of Top-hat Laser Beam Processing and Scanning Strategies in Laser Micro-Structuring, *Micromachines (Basel)*, p. 221, Feb. 2020, doi: 10.3390/MI11020221.

[26] A. Schmickler, K. Braun, A. Temmler et al., Glass processing with pulsed CO_2 laser radiation, *App. Opt.*, pp. 777–783, Feb. 2017, doi: 10.1364/AO.56.000777.

[27] D. J. Hwang, T. Y. Choi, and C. P. Grigoropoulos, Liquid-assisted femtosecond laser drilling of straight and three-dimensional microchannels in glass, *Appl. Phys. A*, pp. 605–612, Aug. 2004, doi: 10.1007/S00339-004-2547-8/METRICS.

[28] J. M. Liu, Simple technique for measurements of pulsed Gaussian-beam spot sizes, *Opt. Lett.*, p. 196, May 1982, doi: 10.1364/OL.7.000196.

[29] Re-evaluated ISO-4827 standard. http://resource.npl.co.uk/softgauges/pdf/Specification.pdf (accessed Jul. 13, 2023).

Santrauka

Aleksandras Kondratas

APDIRBIMO PRODUKTŲ PAŠALINIMO METODAI FREZUOJANT LYDYTĄ KVARCĄ NUO APATINĖS PUSĖS PIKOSEKUNDINIAIS LAZERIO IMPULSAIS

Lazerinis apdirbimas leidžia sparčiai suformuoti mažų dydžių bei aukštos kokybės paviršius. Įprastai lazeriniame apdirbime naudojama tiesioginė abliacija, kur pluoštas yra fokusuojamas į viršutinį paviršių. Tačiau dėl suformuojamo apdirbimo sienelių kampo, šis būdas nėra tinkamas didelio gylio ir diametro santykio kanalų gręžimui. Fokusuojant pluoštą į apatinę bandinio pusę išvengiamas pluošto išsklaidymas nuo jau suformuotų kanalų sienelių. Todėl šiuo būdu galima suformuoti lygiagrečias sieneles ir pasiekti didesnį kanalo gylio ir diametro santykį. Formuojant mažo diametro kanalus svarbu, jog apdirbimo produktai būtų pašalinti iš apdirbimo zonos ir neužkimštų kanalo. Norint suformuoti gilesnius kanalus, reikalingas papildomas apdirbimo produktų pašalinimas iš apdirbimo vietos. Šis darbas atliktas norint išsiaiškinti, kuris apdirbimo produktų pašalinimo būdas yra veiksmingiausias kanalų formavimui.

Darbo tikslas – ištirti kanalų frezavimą naudojant 1064 nm bangos ilgio pikosekundinį lazerį fokusuojant pluoštą į apatinę lydyto kvarco pusę panaudojant skirtingus dulkių pašalinimo metodus.

Eksperimento metu pastebėta, kad kanalų formavimui itin svarbu apdirbimo produktų pašalinimas iš apdirbimo zonos, tai leidžia pasiekti didesnio gylio kanalus su didesne frezavimo sparta.

Mažiausi 300 μm diametro kanalai suformuoti naudojant pastovų oro pūtimą link apdirbimo zonos frezuojant 6,3 mm lydytą kvarcą. Su kitais apdirbimo produktų pašalinimo metodais mažiausi diametrai buvo du arba daugiau kartų didesni.

Mažesni nei 100 μm diametro kanalai išfrezuoti naudojant pastovų pūtimą ant 1 mm storio lydyto kvarco.

Bandinio panardinimas į vandenį leido suformuoti didžiausio kampo 1 mm diametro kanalus 6,3 mm lydyto kvarco bandinio storyje. Apdirbimo produktų pašalinimas vandeniu leido suformuoti 24 laipsnių kampo kanalus, o pūtimas link bandinio 14 – 15 laipsnių.